

## *Supporting Information*

### **Nanocrystalline anatase TiO<sub>2</sub>/reduced graphene oxide composite films as photoanodes for photoelectrochemical water splitting studies: the role of the reduced graphene oxide**

Andreia Morais, Claudia Longo, Joyce R. Araujo, Monica Barroso, James R. Durrant, Ana Flavia Nogueira\*

#### **S1. Synthesis and characterization of RGO**

##### **S1.1. Synthesis of graphene oxide and reduced graphene oxide**

Graphene oxide (GO) was synthesized from natural graphite powder using a modified Hummers and Offeman's method.<sup>1,2</sup> The graphite powder (10 g) was added to a mixture of concentrated H<sub>2</sub>SO<sub>4</sub> (60 mL), K<sub>2</sub>S<sub>2</sub>O<sub>8</sub> (5 g) and P<sub>2</sub>O<sub>5</sub> (5 g). The dispersion was stirred for 6 h at 80 °C. The mixture was then carefully diluted, filtered and washed several times using distilled water until pH became neutral. The product was dried in air at ambient temperature overnight. The pre-oxidized graphite powder was added to a mixture of concentrated H<sub>2</sub>SO<sub>4</sub> (200 mL) and NaNO<sub>3</sub> (5 g) under vigorous stirring, and the solution was cooled to 0 °C. Next, 15 g of KMnO<sub>4</sub> was added gradually under stirring and the temperature of the mixture was kept below 20 °C. The mixture was stirred at 40 °C for 4 h, and then diluted with distilled water (2 L) in an ice bath. The reaction was terminated by the addition of 30 % (v/v) H<sub>2</sub>O<sub>2</sub> solution (50 mL). The mixture was filtered and washed with 3 % (v/v) H<sub>2</sub>SO<sub>4</sub> solution in order to remove metal ions. The final product (graphite oxide) was suspended in distilled water to give a viscous and brown dispersion, which was subjected to dialysis to completely remove metal ions and acids. The lyophilized graphite oxide was used in the characterization procedure and the resulting GO dispersion (1.8 % w/w) was used in the preparation of the nanocrystalline TiO<sub>2</sub>/RGO pastas.

For reduction of GO, firstly, 200 mg of GO dispersion (1.8 % w/w) was dispersed in distilled water (100 mL) using ultrasonic bath for 30 min. Then, the aqueous dispersion was autoclaved at 220 °C for 12 h to promote the reduction of GO into RGO. The obtained black material was filtered off and dried under vacuum (70 °C).<sup>3</sup> The final product was designated as RGO-hydrothermal.

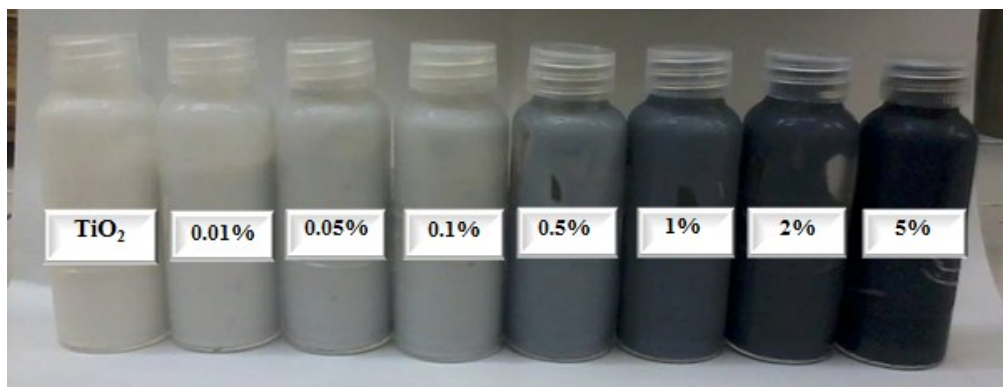


**Fig. S1.** TiO<sub>2</sub> pastes containing different RGO concentrations, ranging from 0 to 5%.

### S1.2. Characterization of graphite, graphite oxide and reduced graphene oxide

Thermogravimetric analysis was performed to investigate all the thermal decomposition steps involved for the graphite, graphite oxide and RGO-hydrothermal samples. The thermal stability of the samples was analyzed on a TA Instruments 2950 thermogravimetric analyzer at a heating rate of 10 °C min<sup>-1</sup>, using a synthetic air stream (100 dm<sup>3</sup> min<sup>-1</sup>) in the temperature range of 50 °C to 1000 °C. The thermogravimetric curves based on the weight loss during the heating in oxidizing atmosphere are shown in Fig. S2.

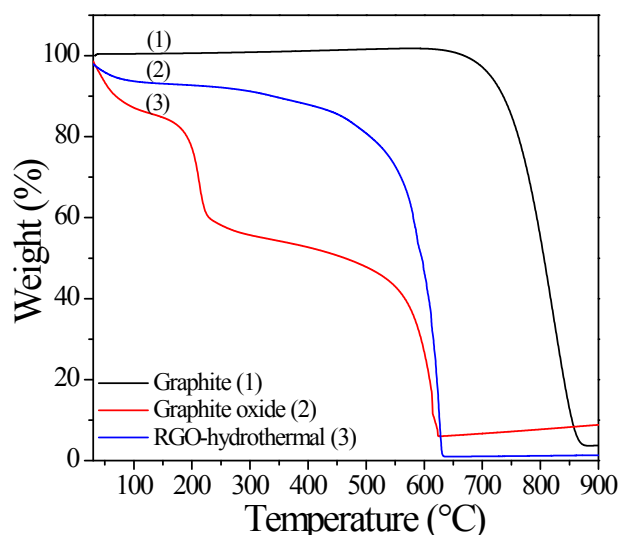


**Fig. S2.** Thermal gravimetric analysis curves for the (a) graphite, (b) graphite oxide and (c) RGO-hydrothermal samples.

For the graphite sample, the thermal decomposition occurs in one step with mass loss (~ 96 %) at about 700 °C. The high thermal stability of this material may be related to its organized and stacked hexagonal structure. Compared with graphite, the graphite oxide and RGO-hydrothermal samples have lower thermal stabilities. These materials are thermally decomposed after three steps. The first mass loss during the initial heating (100 °C) refers to the removal of water molecules trapped between the sheets. For the graphite oxide sample, the second mass loss is observed at about 170 °C with a considerable mass loss (~ 25 %) assigned to the pyrolysis of the labile oxygen-containing functional groups. The same mass loss was also observed for the RGO-hydrothermal sample, however, it was not so pronounced. In this case, even after the hydrothermal reduction process, total elimination of oxygen-containing functional groups does not occur

and for this reason the behavior of this sample is an intermediate between the graphite and the graphite oxide. The major mass loss ( $\sim 40\%$ ) for graphite oxide occurs in a temperature range from  $530\text{ }^{\circ}\text{C}$  to  $630\text{ }^{\circ}\text{C}$ , which was attributed to the combustion of the carbon skeleton of GO. For the sample of RGO-hydrothermal, this third mass loss ( $\sim 80\%$ ) occurs at  $\sim 500\text{ }^{\circ}\text{C}$ . This characterization method was very useful for checking the stability of the synthesized carbonaceous materials with increasing temperature.

X-ray photoelectron analyses (XPS) was used to determine the chemical composition of the graphite, graphite oxide and RGO-hydrothermal samples. The XPS were carried out in an ultra-high vacuum station (Escapulus P System, Omicron Nanotechnology, Taunusstein, Germany) with pressure in the measurement chamber of 10-10 mbar, using an Al X-ray source ( $K\alpha = 1486.7\text{ eV}$ ), with power given by emission of 16 mA, at a voltage of 15 kV. For the individual peak regions were used analyzer pass energy of 20 eV and step of 0.05 eV. Survey spectrum was measured at 70 eV analyzer pass energy. The binding energies were referred to the carbon 1s level, set as 284.6 eV. Analyses of the peaks were performed with the CasaXPS software, using a weighted sum of Lorentzian and Gaussian components curves after performing a Shirley background subtraction. Samples of graphite, lyophilized graphite oxide and RGO-hydrothermal were pressed on a silicon tape (Kapton) and subjected to analysis (XPS).

XPS survey spectra (0 to 1000 eV) were obtained to identify and quantify the elements and chemical groups present in these samples, as shown in Fig. S3.

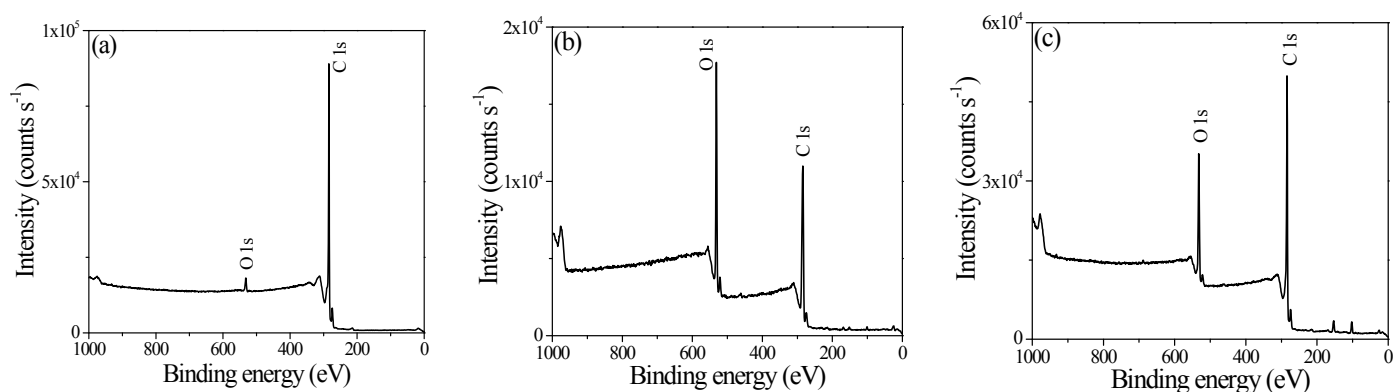


**Fig. S3.** XPS survey spectra for the (a) graphite, (b) GO and (c) RGO-hydrothermal samples, showing the chemical elements in each sample.

The spectra showed essentially the presence of the elements: carbon (C 1s) and oxygen (O 1s) in the region around 284 eV and 532 eV, respectively. Quantification of atomic percentages from XPS spectra is done selecting one transition (the most intense transition) per element. In this case, we use the C 1s and O 1s core level transitions to evaluate the atomic concentrations. Atomic percentages using CasaXPS were evaluated dividing the peak areas above the background by the Relative Sensitivity Factors (RSF) for each element, equation 1. Relative sensitivity factors are dependent on the X-ray source used (Al  $K\alpha$ , in our case) and element analyzed. In this work, we used the RSF values for carbon and oxygen 1.00 and 2.93, respectively, as indicated by CasaXPS software for Al X-ray source. Table S1 shows the values of the binding energies, atomic percentage (at %), and the full width at half maximum (FWHM) obtained from each XPS survey spectrum, corresponding to predominant chemical elements, carbon and oxygen.

$$At\%_C = \frac{(Peak\ Area_C/RSF_C)}{Peak\ Area_C/RSF_C + Peak\ Area_O/RSF_O} \cdot 100 \quad (1)$$

**Table S1.** Summary of the XPS binding energies, FWHM (in eV) and atomic percentages for the chemical elements found in graphite, graphite oxide and RGO-hydrothermal, at contents higher than 1 at %.

Sample	Element	Binding energy (eV)	FWHM	at %
Graphite	C	284.6	2.4	97.4
	O	531.8	4.0	2.6
Graphite oxide	C	284.6	4.6	73.9
	O	531.6	3.1	26.1
RGO-hydrothermal	C	284.6	2.6	82.9
	O	532.6	3.4	17.1

In the RGO-hydrothermal sample, the C percentage was 82.9 at % (and 17.1 at% of O), against 97.4 at % in the graphite sample, showing that the graphite structure was not totally recovered. However, such difference is considered small (in the graphite oxide sample, the C and O percentages were 73.9 and 26.1 at %, respectively). According to these data, the C/O ratios were 37.5 and 2.8 for the graphite and graphite oxide samples, respectively. This is an indication that functional groups containing oxygen were introduced in the pristine graphite after the oxidation process. For the RGO-hydrothermal sample, the C/O ratio was 4.8, showing that there was a small increase in this ratio due to partial removal of functional groups containing oxygen after the hydrothermal method. High resolution XPS C1s spectra obtained for these samples are shown in Fig S4.

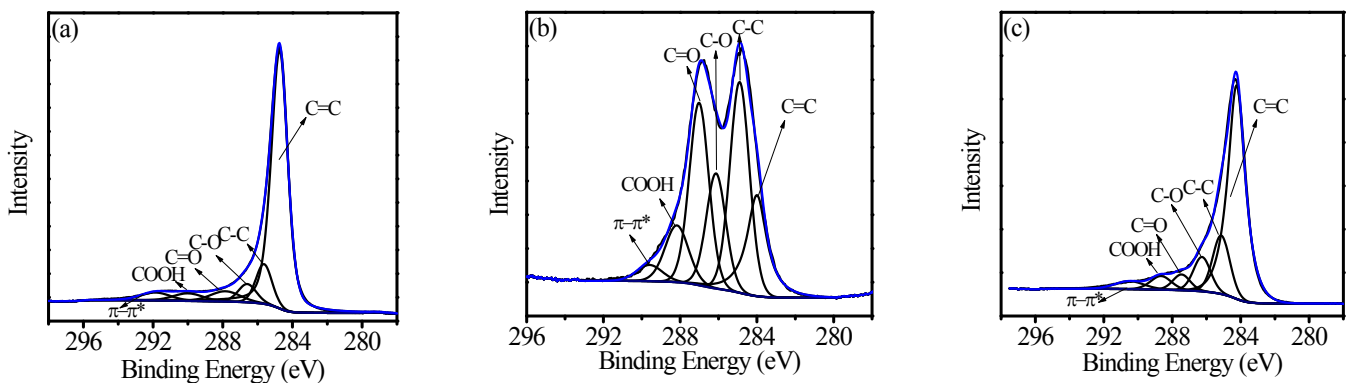


**Fig. S4.** XPS spectra of the region of carbon (C1s) for the (a) graphite, (b) graphite oxide and (c) RGO-hydrothermal samples.

The XPS C1s peak of the graphite (Fig. S4(a)) can be decomposed in six components which correspond to the following functional groups:  $sp^2$ -hybridized carbon (C=C,  $284.2 \pm 0.2$  eV),  $sp^3$ -hybridized carbon (C-C,  $284.9 \pm 0.2$  eV), hydroxyl/phenols/epoxy/ether (C-OH/C-O-C,  $286.1 \pm 0.2$  eV), carbonyl (C=O,  $287.5 \pm 0.5$  eV), carboxyl (HO-C=O, 288.7 eV) and a shake-up satellite peak ( $\pi \rightarrow \pi^*$ ,  $\sim 291.0$  eV), characteristic of delocalized  $sp^2$  electrons in aromatic C structure.<sup>4,5</sup> After

the oxidation of the graphite sample (Fig. S4(b)), the peaks related to the functional groups containing oxygen were enlarged and become more evident. The XPS C1s analysis suggests that the final product (graphite oxide) contains a large number of functional groups in its surface such as epoxy, carbonyl, hydroxyl and carboxyl groups.

The XPS spectrum of the RGO-hydrothermal sample (Fig. S4(c)) resembles the spectrum of the graphite (Fig. S4(a)), and the peaks related to the oxygen containing functional groups are much less intense. Through this analysis, it was possible to demonstrate the presence of oxygen functional groups on the surface even after reduction process by hydrothermal method, indicating that the GO was not fully reduced.<sup>44-46</sup> Another interesting fact can be evidenced in Table S2 where the concentration of C=C bonds (~ 50 %) found in the RGO-hydrothermal sample is similar to the graphite sample (~ 63 %). This is another evidence of almost complete restoration of the sp<sup>2</sup>-hybridized network in the RGO samples.

**Table S2.** Summary of XPS C1s data obtained from fitting calculations regarding the binding energy values, full width at half maximum (FWHM), percentage of each component, and their respective assignments.

Samples	Assignment	Binding energy (eV)	FWHM	at %
Graphite	C=C	284.2	1.1	73.4
	C-C	285.1	1.1	9.8
	C-OH / C-O-C	286.1	1.2	5.1
	C=O	287.3	1.2	4.7
	O-C=O	288.7	1.5	3.4
	$\pi$ - $\pi$ *	291.4	2.0	3.6
Graphite oxide	C=C	284.0	1.2	17.2
	C-C	284.9	1.2	29.2
	C-OH / C-O-C	286.1	1.2	16.0
	C=O	287.1	1.2	25.3
	O-C=O	288.7	1.5	9.4
	$\pi$ - $\pi$ *	290.5	2.0	2.9
RGO-hydrothermal	C=C	284.2	1.2	63.5
	C-C	285.1	1.2	15.4
	C-OH / C-O-C	286.3	1.2	9.1
	C=O	287.5	1.2	4.2
	O-C=O	288.7	1.4	4.3
	$\pi$ - $\pi$ *	290.5	2.0	3.5

We characterized the crystal structure of the same materials by XRD. The results obtained are presented in Fig. S5.

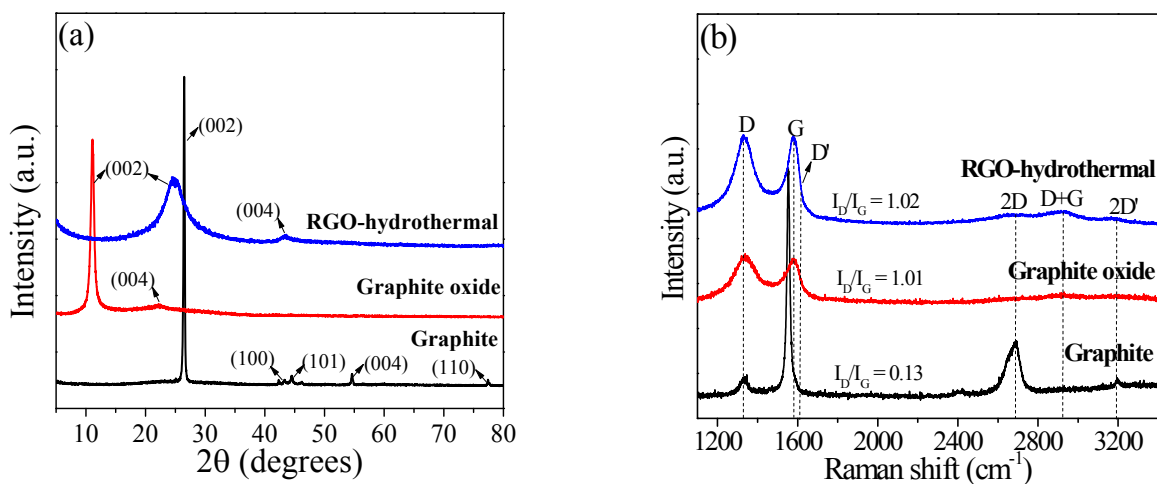


**Fig. S5.** XRD patterns (a) and Raman spectra (b) of graphite, graphite oxide and RGO-hydrothermal samples.

The XRD pattern of graphite powder exhibits an intense characteristic peak at  $2\theta = 26.6^\circ$  corresponding to an interplanar spacing of  $d(002) = 3.35 \text{ \AA}$ , followed by the weak (100), (101), (004) and (110) reflection peaks at  $2\theta = 43.3^\circ$ ,  $44.5^\circ$ ,  $54.6^\circ$  and  $77.4^\circ$ , respectively.<sup>6</sup> After the oxidation of graphite into graphite oxide, the  $2\theta$  peak position (002) shifts to  $11.1^\circ$  and the interplanar spacing increases to  $d(002) = 8.0 \text{ \AA}$ . This phenomenon can be attributed to the introduction of oxygen-containing functional groups and water molecules into the carbon lattice during the oxidation.<sup>7</sup> When the graphite oxide is treated by a hydrothermal process, the  $2\theta$  peak at  $11.1^\circ$  disappears and a broader and weaker peak centred at around  $2\theta = 25^\circ$  with a interplanar spacing of  $d(002) = 3.37 \text{ \AA}$  appears implying that the oxygen-containing functional groups of graphite oxide were partially removed and without adding any reducing agent. There is also a noticeable decrease in the intensity of the diffraction peak due to loss of crystallinity of the material, with formation of more disordered, less packing structures.<sup>8</sup>

The Raman spectra (Fig. S5(b)) for the graphite, graphite oxide and RGO-hydrothermal samples showed two major vibrational modes in positions close to  $1330 \text{ cm}^{-1}$  and  $1581 \text{ cm}^{-1}$  corresponding to D and G bands, respectively. The G band is related to the  $E_{2g}$  vibration mode of  $sp^2$  carbon domains and can be used to explain the degree of graphitization, whereas the D band is associated with structural defects and partially disordered structures of the  $sp^2$  domains. The spectra also show the presence of other bands of lower intensity associated with  $D'$ , 2D (or  $G'$ ),  $D+D$  and  $2D'$  bands, around  $1610 \text{ cm}^{-1}$ ,  $2680 \text{ cm}^{-1}$ ,  $2925 \text{ cm}^{-1}$  and  $3200 \text{ cm}^{-1}$ , respectively. The intensity ratio between the D and G bands ( $I_D/I_G$ ) is often used as a parameter to correlate the disorder degree in the carbonaceous materials.<sup>9</sup>

According to Fig. S5(b), the graphite sample was observed that the intensity of the D band is lower than the G band, indicating that the structure is quite orderly. In this case, the graphite have few structural defects, and the  $I_D/I_G$  ratio is near zero ( $I_D/I_G = 0.13$ ). After the oxidation process, a prominent D band

appears due to the increased presence of structural defects caused mainly by introduction of functional groups ( $I_D/I_G = 1.01$ ). The Raman spectrum of the RGO-hydrothermal sample also contains the same vibrational modes and the  $I_D/I_G$  intensity ratio is slightly larger ( $I_D/I_G = 1.02$ ) compared to the graphite oxide sample. This suggests that a small increase of the intensity of the D band is associated with the presence of residual functional groups in its structure, as shown in the XPS spectra of the C 1s.

The morphological characterization of the graphite, graphite oxide and RGO-hydrothermal samples was carried out through FEG-SEM and HRTEM, as shown in the Fig. S6.

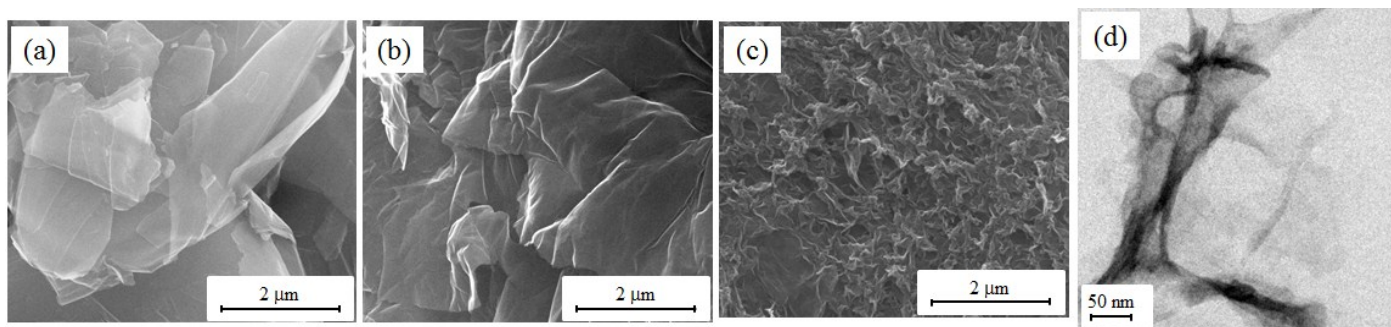


**Fig. S6.** FEG-SEM images for the (a) graphite, (b) graphite oxide and (c) RGO-hydrothermal samples. (d) HRTEM images for the RGO-hydrothermal samples.

For the graphite sample (Fig. S6(a)), it was possible to observe the ordered structures consisting of aggregates containing regularly spaced lamellae of different sizes. The morphology of the graphite oxide (Fig. S6(b)) consists of layered and disordered structures, very much like those already reported in the literature.<sup>10-12</sup> After the reduction process by hydrothermal method, the RGO sheets have poor colloidal stability and therefore their tendency is to form agglomerates with transparent, fine and curled sheets. This can be clearly observed by FEG-SEM and HRTEM images in Fig. S6(c) and S6(d), respectively.

## S2. Characterization of TiO<sub>2</sub> and TiO<sub>2</sub>/RGO films deposited on glass-FTO

Fig. S7 shows the optical microscope images of the TiO<sub>2</sub> and TiO<sub>2</sub>/RGO films.

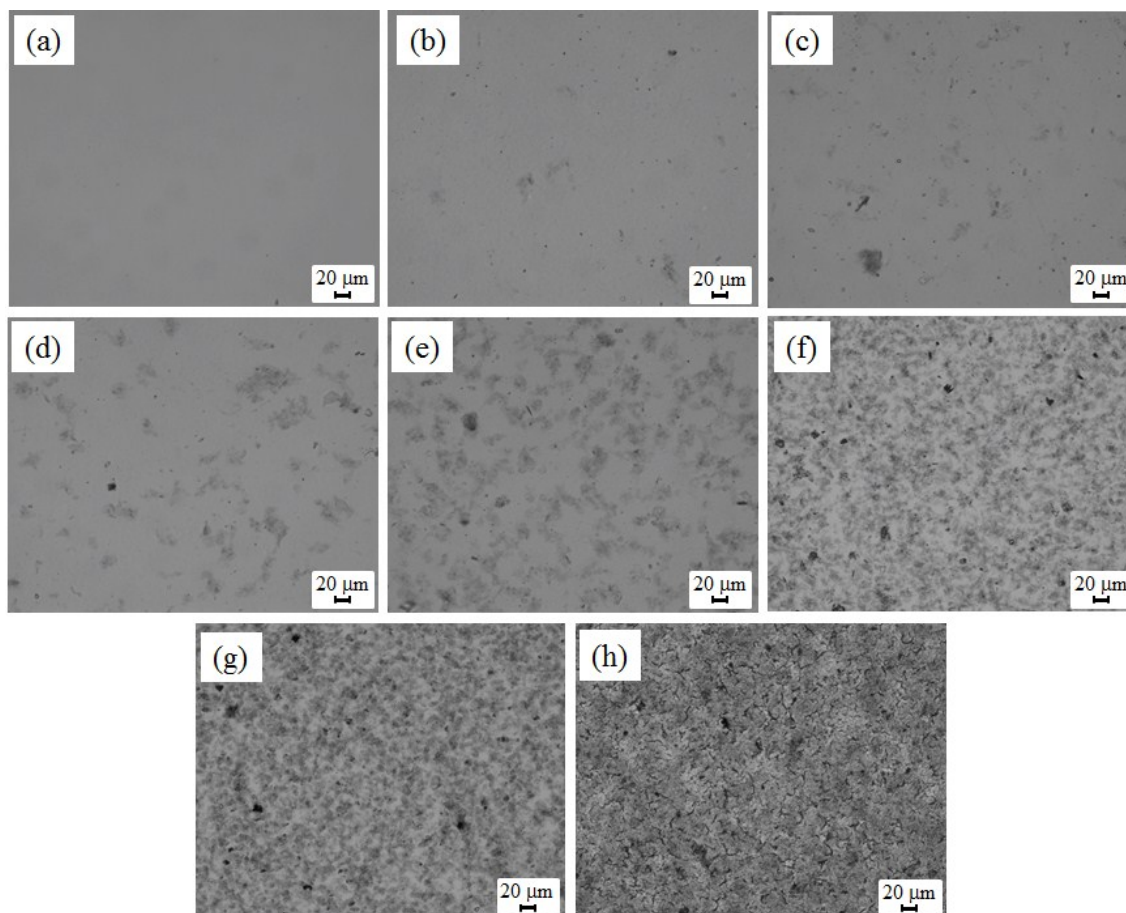


Fig. S7. Optical microscopy images of the TiO<sub>2</sub> and TiO<sub>2</sub>/RGO films.

The UV-visible absorption spectra of the TiO<sub>2</sub> and TiO<sub>2</sub>/RGO films (Fig. S8) were measured with an Agilent Technologies Cary 60 UV-Vis spectrophotometer.

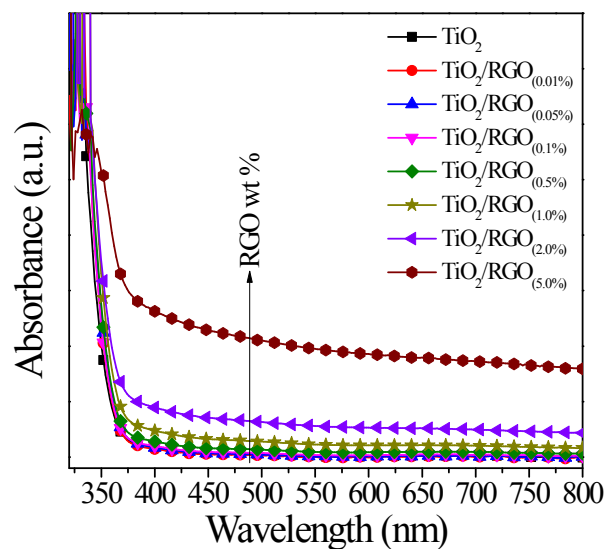


Fig. S8. UV-visible absorption spectra for the TiO<sub>2</sub> and TiO<sub>2</sub>/RGO films.

### S3. Electrochemical properties of TiO<sub>2</sub> and TiO<sub>2</sub>/RGO films deposited on glass-FTO

The cyclic voltammogram, obtained in a wide potential range (0.4 to 2.4 V<sub>RHE</sub>), of the TiO<sub>2</sub> electrode in the dark is shown in Fig. S9. The redox reaction may be represented as follows:<sup>13</sup>

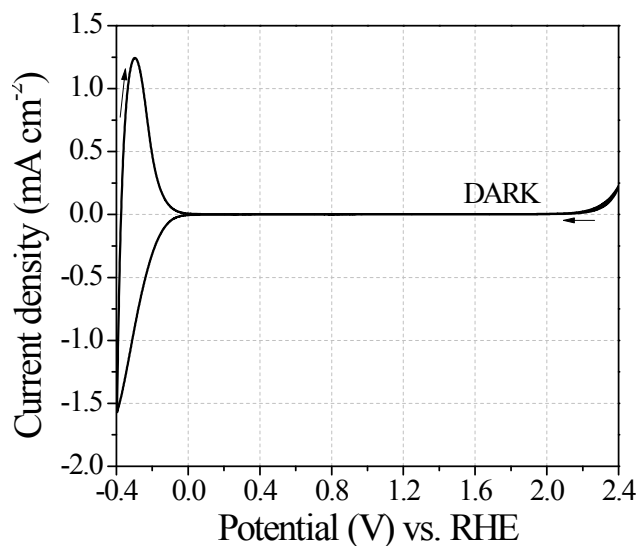
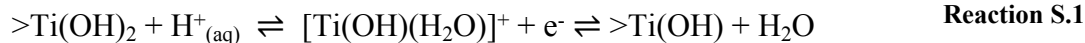


Fig. S9. Cyclic voltammogram of the TiO<sub>2</sub> electrode in 0.50 mol L<sup>-1</sup> H<sub>2</sub>SO<sub>4</sub>, in the dark and potential scan rate of 20 mV s<sup>-1</sup>.

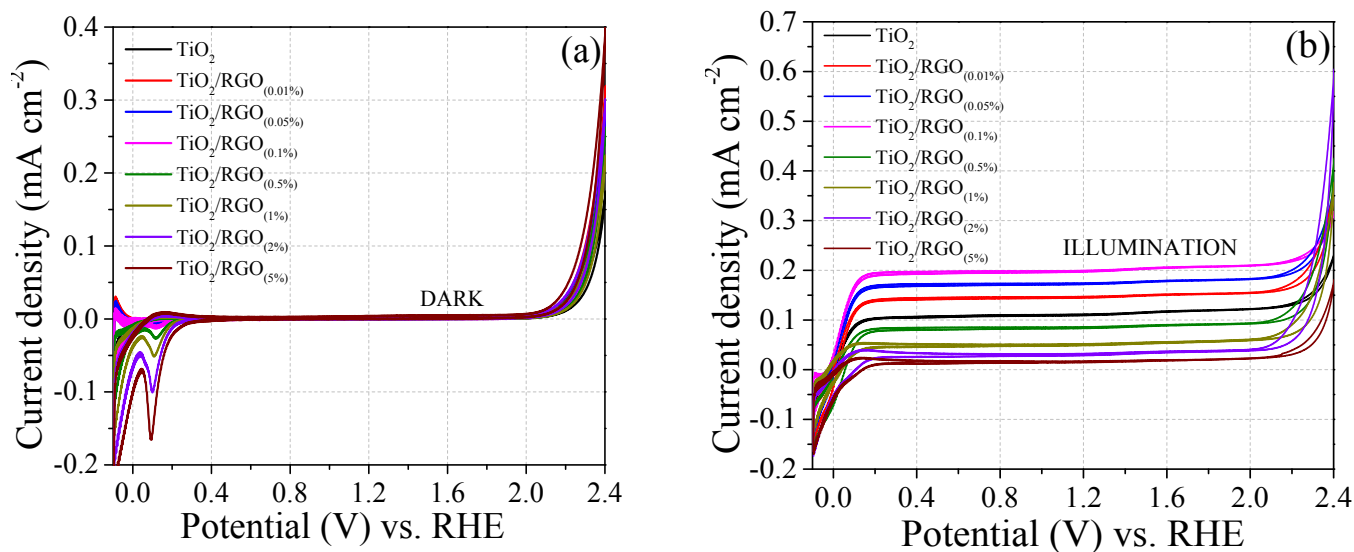
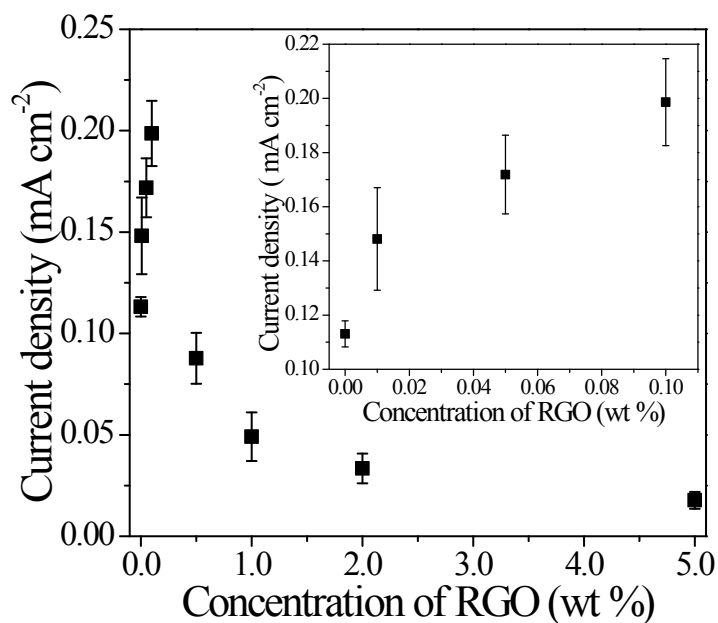
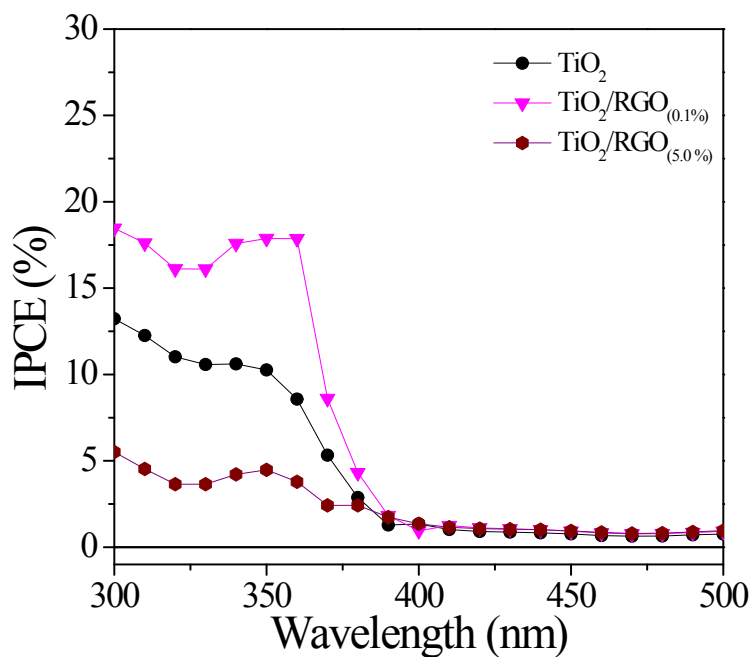


Fig. S10. Cyclic voltammograms obtained using the TiO<sub>2</sub> and TiO<sub>2</sub>/RGO films as photoanodes in 0.5 mol L<sup>-1</sup> H<sub>2</sub>SO<sub>4</sub>, (a) in the dark and (b) under illumination.

Five films for each concentration of RGO were used in this study and then, the averages and standard deviations of the photocurrent densities at 1.23 V<sub>RHE</sub> (standard potential for OER) obtained for were calculated and presented in Fig. S11.



**Fig. S11.** Variation of photocurrent density values (at 1.23 V<sub>RHE</sub>) with the relative concentration of RGO in the composite TiO<sub>2</sub>/RGO films electrodes (n = 5) in aqueous H<sub>2</sub>SO<sub>4</sub> solution, under polychromatic irradiation.



**Fig. S12.** IPCE spectra for the TiO<sub>2</sub>, TiO<sub>2</sub>/RGO<sub>(0.1%)</sub> and TiO<sub>2</sub>/RGO<sub>(5%)</sub> electrodes, under potentiostatic control at 1.23 V<sub>RHE</sub>

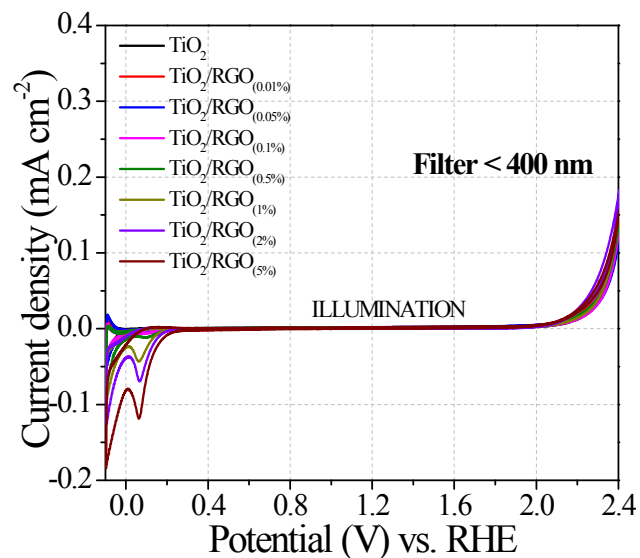


**Fig. S13.** Cyclic voltammogram of the  $\text{TiO}_2$  and  $\text{TiO}_2/\text{RGO}$  electrodes in  $0.50 \text{ mol L}^{-1} \text{ H}_2\text{SO}_4$ , under illumination, using an UV blocking filter ( $< 400 \text{ nm}$ ) and potential scan rate of  $20 \text{ mV s}^{-1}$ .

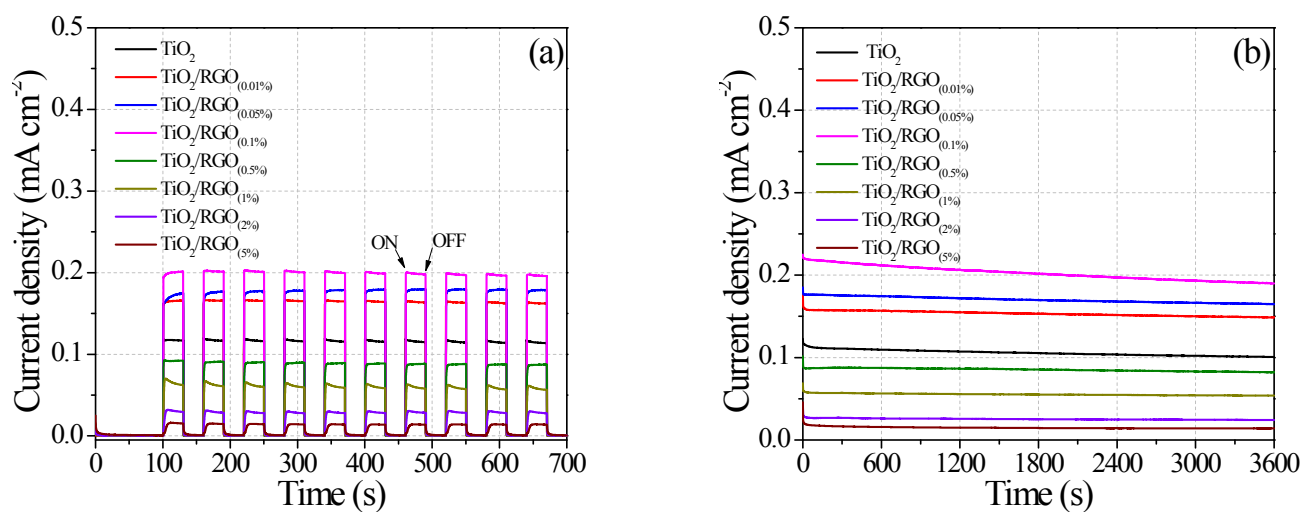


**Fig. S14.** Time-dependent photocurrent density under potentiostatic control at  $1.23 \text{ V}_{\text{RHE}}$ , under intermittent irradiation using a manual chopper with intervals of  $30 \text{ s}$  in the dark and  $30 \text{ s}$  under irradiation (a) and under continuous irradiation (b) for the  $\text{TiO}_2$  and  $\text{TiO}_2/\text{RGO}$  photoelectrodes in  $0.5 \text{ mol L}^{-1} \text{ H}_2\text{SO}_4$ .

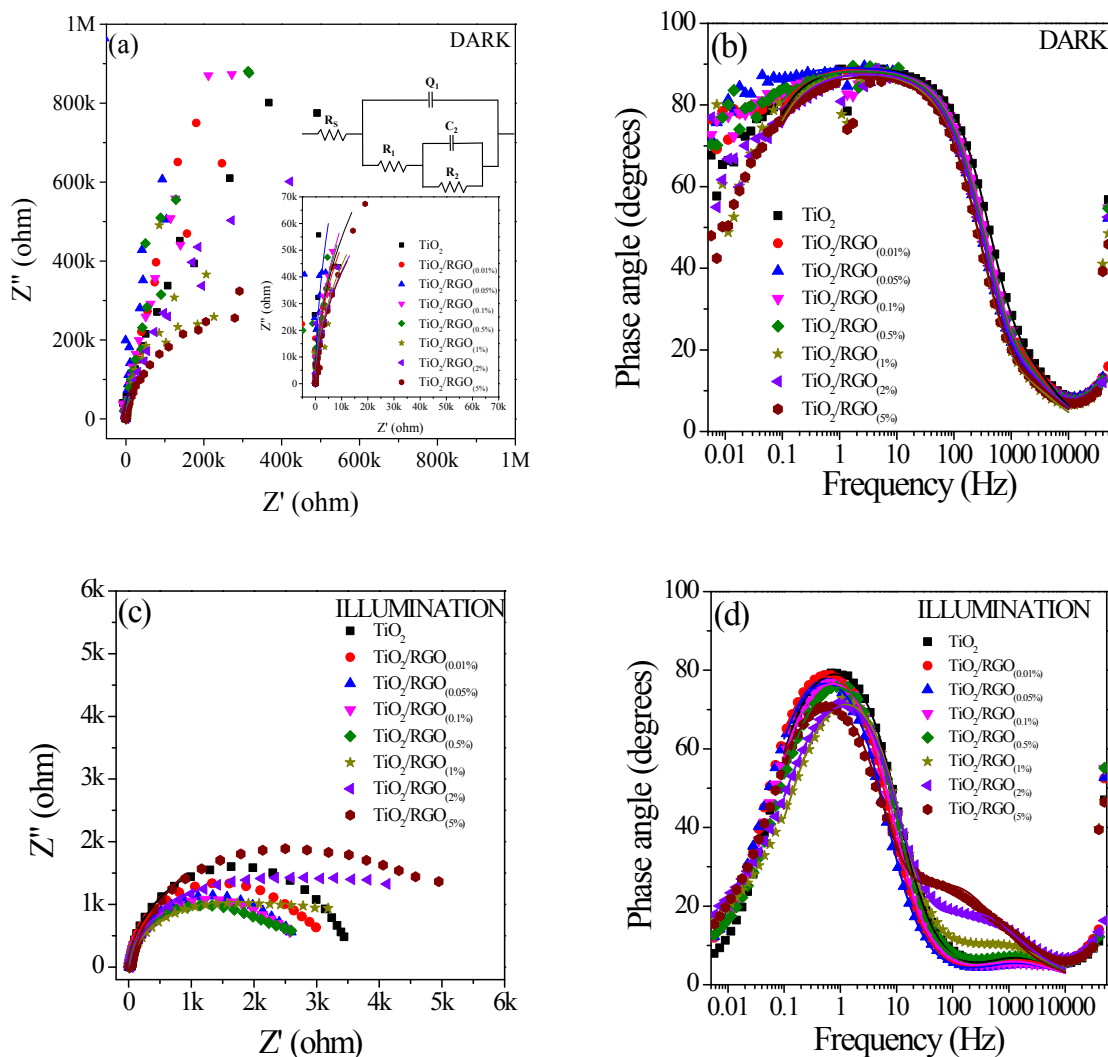


**Fig. S15.** (a) (b) Nyquist and (c) (d) Bode (phase angle versus frequency) diagrams of the EIS data obtained for the TiO<sub>2</sub> and TiO<sub>2</sub>/RGO photoelectrodes at open circuit potential, in 0.5 mol L<sup>-1</sup> H<sub>2</sub>SO<sub>4</sub> in the dark (a) (b) and under illumination (c) (d). The symbols correspond to the experimental data and solid lines represent the fits obtained using the Boukamp software. The equivalent circuit inserted in Fig. S16(a).

## References

- <sup>1</sup>Kovtyukhova, N. I., Ollivier, P. J., Martin, B. R., Mallouk, T. E., Chizhik, S. A., Buzaneva, E. V. and Gorchinskiy, A. D. Layer-by-layer assembly of ultrathin composite films from micron-sized graphite oxide sheets and polycations. *Chemistry of Materials*. **1999**, 11, 771-778.
- <sup>2</sup>Hummers, W. S. and Offeman, R. E. Preparation of Graphitic Oxide. *Journal of the American Chemical Society*. **1958**, 80, 1339-1339.
- <sup>3</sup>Ding, J. N., Liu, Y. B., Yuan, N. Y., Ding, G. Q., Fan, Y. and Yu, C. T. The influence of temperature, time and concentration on the dispersion of reduced graphene oxide prepared by hydrothermal reduction. *Diamond and Related Materials*. **2012**, 21, 11-15.
- <sup>4</sup>Filik, J., May, P. W., Pearce, S. R. J., Wild, R. K. and Hallam, K. R. XPS and laser Raman analysis of hydrogenated amorphous carbon films. *Diamond and Related Materials*. **2003**, 12, 974-978.
- <sup>5</sup>Hsiao, M. C., Liao, S. H., Yen, M. Y., Teng, C. C., Lee, S. H., Pu, N. W., Wang, C. A., Sung, Y., Ger, M. D., Ma, C. C. M. and Hsiao, M. H. Preparation and properties of a graphene reinforced nanocomposite conducting plate. *Journal of Materials Chemistry*. **2010**, 20, 8496-8505.
- <sup>6</sup>Li, Z. Q., Lu, C. J., Xia, Z. P., Zhou, Y. and Luo, Z. X-ray diffraction patterns of graphite and turbostratic carbon. *Carbon*. **2007**, 45, 1686-1695.
- <sup>7</sup>Wang, H. and Hu, Y. H. Effect of Oxygen Content on Structures of Graphite Oxides. *Industrial & Engineering Chemistry Research*. **2011**, 50, 6132-6137.
- <sup>8</sup>Shen, J. F., Yan, B., Shi, M., Ma, H. W., Li, N. and Ye, M. X. One step hydrothermal synthesis of TiO<sub>2</sub>-reduced graphene oxide sheets. *Journal of Materials Chemistry*. **2011**, 21, 3415-3421.

- <sup>9</sup>Some, S., Bhunia, P., Hwang, E., Lee, K., Yoon, Y., Seo, S. and Lee, H. Can Commonly Used Hydrazine Produce n-Type Graphene? *Chemistry-a European Journal*. **2012**, 18, 7665-7670.
- <sup>10</sup>Stankovich, S., Dikin, D. A., Piner, R. D., Kohlhaas, K. A., Kleinhammes, A., Jia, Y., Wu, Y., Nguyen, S. T. and Ruoff, R. S. Synthesis of graphene-based nanosheets via chemical reduction of exfoliated graphite oxide. *Carbon*. **2007**, 45, 1558-1565.
- <sup>11</sup>Zhou, Y., Bao, Q. L., Tang, L. A. L., Zhong, Y. L. and Loh, K. P. Hydrothermal Dehydration for the "Green" Reduction of Exfoliated Graphene Oxide to Graphene and Demonstration of Tunable Optical Limiting Properties. *Chemistry of Materials*. **2009**, 21, 2950-2956.
- <sup>12</sup>Park, S., An, J., Potts, J. R., Velamakanni, A., Murali, S. and Ruoff, R. S. Hydrazine-reduction of graphite- and graphene oxide. *Carbon*. **2011**, 49, 3019-3023.
- <sup>13</sup>Oliva, F. Y., Avalle, L. B., Santos, E. and Camara, O. R. Photoelectrochemical characterization of nanocrystalline TiO<sub>2</sub> films on titanium substrates. *Journal of Photochemistry and Photobiology A-Chemistry*. **2002**, 146, 175-188.